

Angle-resolved three-dimensional analysis of surface films by coherence scanning interferometry

Peter de Groot* and Xavier Colonna de Lega

Zygo Corporation, Middlefield, Connecticut 06455, USA

*Corresponding author: peterd@zygo.com

Received January 16, 2007; revised April 18, 2007; accepted April 20, 2007;
posted April 27, 2007 (Doc. ID 78989); published June 5, 2007

The Fourier components of interference signals generated by scanning a high-numerical-aperture objective orthogonal to an object surface correspond to different angles of incidence on the surface. The phase and amplitude of these Fourier components relate to the structure of the object, including in particular the 3D topography and thickness profiles of thin-film layers. © 2007 Optical Society of America

OCIS codes: 120.3180, 120.6650, 150.6910, 180.3170, 240.0310.

Many commercially important devices in semiconductor wafers, flat panel displays, and micromechanical and telecommunication systems are composed of semitransparent thin films. The metrology of thin films is a key part of the manufacturing process control for these devices.

The workhorses for film thickness analysis are the ellipsometer and its unpolarized cousin, the reflectometer. These instruments work at multiple wavelengths, multiple incident angles, or both. An approach to rapidly collecting data over a wide range of angles is to image the pupil (or back focal plane) of a high-numerical-aperture (NA) microscope objective onto a camera [1]. High-NA, pupil-plane imaging provides the angle-resolved optical properties of surfaces at a single, focused measurement point [2–4].

Often it is desirable to go beyond a single-point thickness measurement and to rapidly generate film profiles as well as other details of the surface structure. Here we present a method for full-field, 3D film profile and top-surface topography using interferometry. Our instrument also relies on a high-NA objective to provide a range of incident angles; however, unlike instruments that directly image the objective pupil, our instrument resolves the angles mathematically by Fourier analysis of the interference signals collected at the image plane. This approach generates angle-resolved reflectometry as well as surface topography data over thousands of image points simultaneously.

The microscope shown in Fig. 1, with its interference objective and piezo-electric transducers (PZT) scanner, is a similar configuration with that used for conventional scanning white light interferometry. Indeed, our approach is comparable with the wavelength-resolved technique for thin films proposed by Kim and Kim [5]. Here, however, in place of a white light source and low-NA objective, a spectrally narrowband (e.g., ≤ 30 nm) LED fills the pupil of a high-NA objective [6]. The high NA results in a cone of illumination angles.

To see how the range of incident angles influences the resulting interference signal, we examine in Fig. 1 a specific ray bundle at an incident angle Ψ and calculate its contribution to the measured intensity as a function of scan position. In passing through the

Mirau interference objective, the ray splits and follows a measurement path of complex transmissivity t and a reference path of complex reflectivity r . The recombined, reflected light reaches a digital camera in a conventional imaging geometry so that each pixel on the camera corresponds to a point on the object surface. The object point has a complex reflectivity $m_{x,y}$ that varies with position x,y in the field of view. The PZT actuator provides a scan ζ over several micrometers to generate the desired signals. The time-averaged intensity contribution for the ray reads as

$$g_{x,y}(\mathbf{K}) = |r(\mathbf{K}) + t(\mathbf{K})m_{x,y}(\mathbf{K})\exp[i\mathbf{K}(\zeta - h_{x,y})]|^2, \quad (1)$$

where $h_{x,y}$ is the local surface height at the position x,y . The interference fringe frequency \mathbf{K} varies as the directional cosine $\beta = \cos(\Psi)$ of the incident angle Ψ :

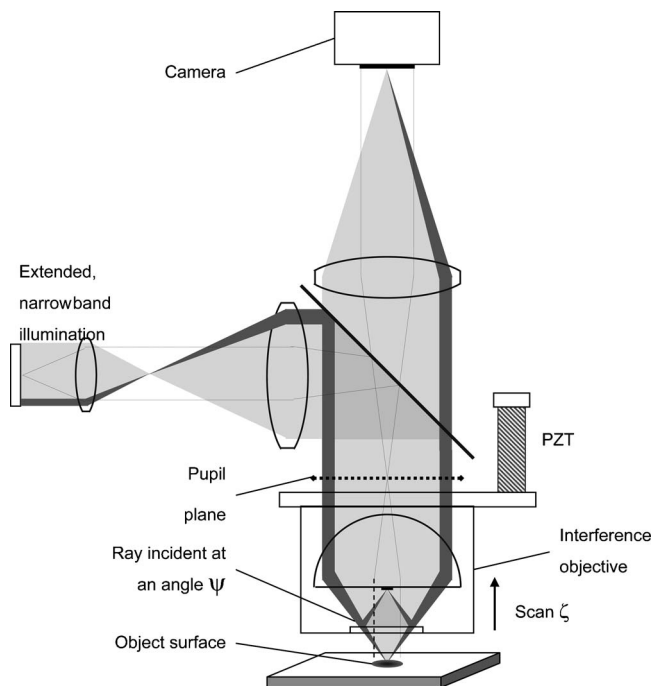


Fig. 1. High-NA, narrow-bandwidth coherence scanning microscope for angle-resolved surface structure analysis. The figure highlights the path of one ray bundle at an incident angle Ψ .

$$K = 4\pi\beta/\lambda. \quad (2)$$

As will become apparent shortly, it is this coupling of frequency K to incident angle Ψ that gives us access to the angle-dependent reflectivity of the sample by frequency analysis of the resultant signal.

The imaging system sums the individual interference patterns over the pupil, leading to a total intensity signal $I_{x,y}$ that can be written as the inverse Fourier transform

$$I_{x,y}(\zeta) = \int_{-\infty}^{\infty} q_{x,y}(K)\exp(-iK\zeta)dK, \quad (3)$$

where the frequency spectrum $q_{x,y}$ is [7]

$$q_{x,y}(K) = \rho(K)\exp(iKh_{x,y}), \quad (4)$$

$$\rho_{x,y}(K > 0) = [KU(K)r(K)t^*(K)/Y]m_{x,y}^*(K), \quad (5)$$

$$Y = \int_{-\infty}^{\infty} U(K)KdK. \quad (6)$$

The symbol $*$ is the complex conjugate operator, and U is the illumination distribution in the pupil plane expressed in terms of frequency K using Eq. (2). Experimentally, $q_{x,y}$ is the forward Fourier transform of the total intensity signal $I_{x,y}$ and the height-independent, positive-frequency coefficients $\rho_{x,y}$ derive from $q_{x,y}$ by subtraction of a linear fit to the phase argument $Kh_{x,y}$.

Figure 2 is a simulation of an interference signal using Eq. (3) for a simple thin film, using a 0.85 NA objective and pure monochromatic light at 500 nm. The localization of fringe contrast at the upper and lower surfaces of the film is related to the large range of angles, which generates a corresponding range of frequencies K that concord only at positions of stationary phase [8,9]. The fringe localization may be thought of as a focus effect—the fringes appear only within the depth of focus of the high-NA lens.

The Fourier transform in Fig. 3 illustrates how these frequencies map to the directional cosine β for the incident angles Ψ . For example, the 500 nm wavelength generates four fringes or interference phase cycles per micrometer at normal incidence (directional cosine $\beta=1$, angle $\Psi=0$), while the same wavelength has reduced fringe frequency at higher

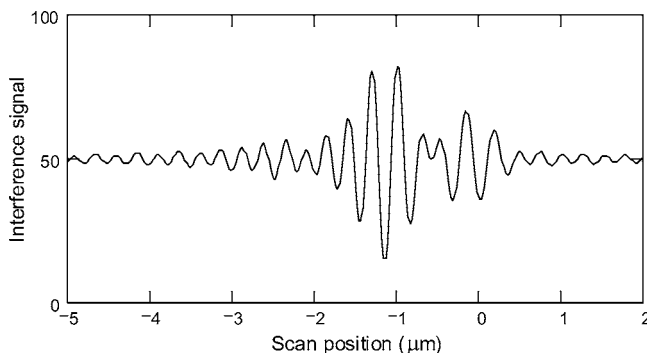


Fig. 2. Simulated interference signal for a 2 μm film of SiO_2 on Si.

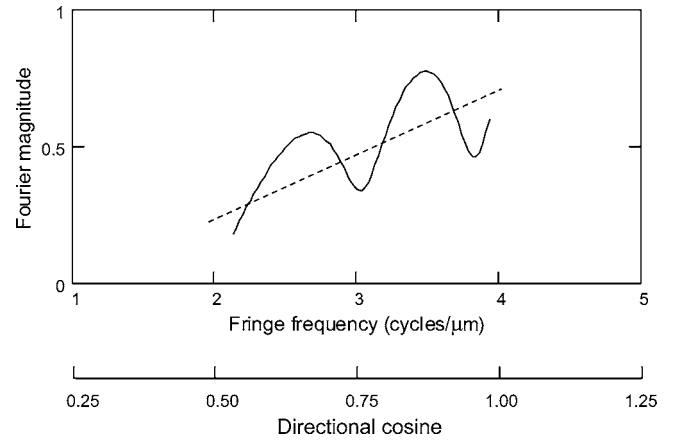


Fig. 3. Fourier transform magnitude of the signal in Fig. 2, showing how the fringe frequencies correspond to the cosines of the incident angles in the high-NA objective. The dashed line is the expected linear spectrum when there is no film on the surface.

incident angles. The nonlinear behavior of the Fourier magnitude is a signature of the film thickness—thicker films generate more oscillations in the spectrum. The Fourier phase is similarly modulated by thin-film effects.

Surface characteristics such as film thickness follow from a comparison of measured Fourier components with the predicted behavior. For example, if the surface is a simple single-layer film, the predicted complex reflectivity \hat{m} as a function of thickness L is

$$\hat{m}(L, K) = \frac{\vartheta_1 + \vartheta_2 \exp(i\bar{K}L)}{1 + \vartheta_1\vartheta_2 \exp(i\bar{K}L)}, \quad (7)$$

where ϑ_1 is the reflectivity of the air–film interface, ϑ_2 is the reflectivity of the film–substrate interface, and

$$\bar{K} = \sqrt{(4\pi/\lambda)^2(n^2 - 1) + K^2} \quad (8)$$

is the interference frequency within the film of index n . The predicted Fourier components are therefore

$$\hat{\rho}(L, K > 0) = [KU(K)r(K)t^*(K)/Y]\hat{m}^*(L, K). \quad (9)$$

A comparison of the measured values $\rho_{x,y}$ with a library of theoretical values $\hat{\rho}$ determines the film thickness $L_{x,y}$. A convenient merit function is a weighted sum of the least-squares difference of the magnitude nonlinearity, the phase nonlinearity, the relative signal strengths, and phase offset differences [6]. Alternatively, the comparison may be done directly by correlation of the predicted signal with the experimental data.

A separate measurement on a well-known artifact having a known reflectivity calibrates for the angle-dependent characteristics U, r, t of the optical system [6]. We can also make use of an area of the object surface itself for this system characterization, if this area is well known and can serve as a reference artifact.

Once we know the film thickness, the surface topography follows from

$$h_{x,y} = \sigma_{x,y} + \frac{1}{K_0} \{A_{x,y} - 2\pi \text{round}[(A_{x,y} - \langle A \rangle) / 2\pi]\}, \quad (10)$$

where $\sigma_{x,y}$ and $A_{x,y}$ are the slope and intercept, respectively, of a linear fit to the material-corrected phase $s_{x,y}$:

$$s_{x,y}(K) = \arg[q_{x,y}(K)] - \arg[\rho_{x,y}(K)]. \quad (11)$$

The frequency K_0 is the centroid of the Fourier magnitude spectrum as determined by the calibration procedure on a film-free artifact. Note that Eq. (10) uses both the slope and the intercept information to calculate a height that has a precision equivalent to or better than phase shifting interferometry, but without fringe ambiguity.

A first experimental verification is a direct measurements of film thickness on SiO₂ on Si standard artifacts that have been independently certified using ellipsometry. Table 1 shows results for nine standards, including a standard deviation based on the noise in the film profile, for an objective NA of 0.78 and a 498 nm, 26 nm bandwidth light source. These results show good agreement with the certified values over the full range.

A second experiment summarized in the cross section of Fig. 4 illustrates the simultaneous acquisition of substrate and top surface profiles and over a film thickness range of 0 to 530 nm of SiO₂ on Si. These data are from a single measurement using a 640 × 480 pixel camera and a 515 nm wavelength LED having a bandwidth of 30 nm. The results illustrate capability down to zero film thickness, although with an increased uncertainty at thinner film thicknesses, for example near 100 nm, that may be improved with a higher-NA objective providing a wider range of incident angles.

The significant benefit of the present approach is the quantity of 3D data for both surface topography and film profiles. However, we would not argue that this technique is competitive with the best ellipsometers optimized for single-point film thickness analysis. Our approach is most attractive for those appli-

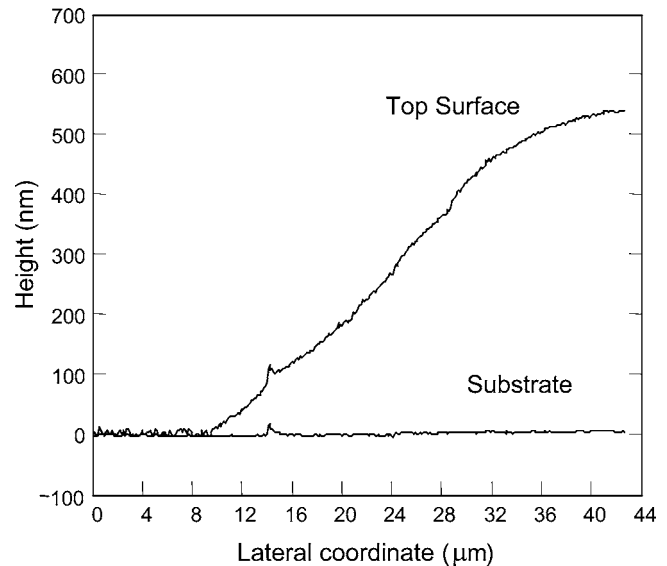


Fig. 4. Experimental cross-sectional profile through a 3D image of the edge of an SiO₂-coated Si wafer. The data show both the Si substrate and top surface of the SiO₂ measured simultaneously over multiple image points.

cations that require this 3D information on simple film stacks for which a relative precision of a few percent is sufficient.

The instrument as described here operates with a narrowband light source, which can be a useful configuration at high magnifications using non-achromatic optics. The basic concept extends to the more general case of nonzero spectral bandwidth using the more extensive mathematical analysis in Ref. [7]. For highest accuracy, we often make use of this more detailed analysis even for narrow-bandwidth light sources where the interference phenomena are dominated by the objective NA but are nonetheless influenced by the spread in wavelengths.

As a concluding remark, an area of continued research is to use this technique for angle-resolved analysis of other surface characteristics such as material differences or optically unresolved surface features.

References

1. M. Pluta, *Advanced Light Microscopy*, Vol. 3 (Elsevier, 1993), pp. 265–271.
2. S. V. Shatalin, R. Juškaitis, J. B. Tan, and T. Wilson, *J. Microsc.* **179**, 241 (1995).
3. A. Rosencwaig, J. Opsal, D. L. Willenborg, S. M. Kelso, and J. T. Fanton, *Appl. Phys. Lett.* **60**, 1301 (1992).
4. G. D. Feke, D. P. Snow, R. D. Grober, P. J. de Groot, and L. Deck, *Appl. Opt.* **37**, 1796 (1998).
5. S.-W. Kim and G.-H. Kim, *Appl. Opt.* **38**, 5968 (1999).
6. P. de Groot, “Interferometry method for ellipsometry, reflectometry, and scatterometry measurements, including characterization of thin film structures,” U.S. patent 7,139,081 (November 21, 2006).
7. P. de Groot and X. Colonna de Lega, *Appl. Opt.* **43**, 4821 (2004).
8. C. J. R. Sheppard and K. G. Larkin, *Appl. Opt.* **34**, 4731 (1995).
9. I. Abdulhalim, *Meas. Sci. Technol.* **12**, 1996 (2001).

Table 1. Measurement Results for SiO₂ on Si Film Thickness Standards

Certified Thickness (nm)	Measured Thickness	Standard Deviation
12.0	16.5	2.7
44.0	36.4	2.2
96.0	96.4	1.4
183.0	186.9	3.6
226.0	218.5	2.3
396.0	390.4	3.2
675.0	672.7	0.9
1003.0	1002.7	1.0
1026.0	1027.3	1.0